Boussinesq modeling of wave processes in field fringing reef environments

Yu Yao (MethodologyInvestigationWriting - original draft) [a c] 👤 ✉, Qiming Zhang (SoftwareValidationVisualization) [a],
Janet M. Becker (Data curationWriting- review & editing) [b], Mark A. Merrifield (ConceptualizationSupervision) [b]

Show more ⌄

≔ Outline | ⌁ Share   ⹂ Cite

Full text access

Highlights

- A Boussinesq model is used to reproduce the wave processes in field reef environments.

- IG waves are generated by breakpoint forcing and normal modes exist across the reef.

- Shoreline SS waves, IG waves and wave setup are larger with concave surfzone seabed.

- Shoreline IG waves are more sensitive to phase variation in incident wave forcing.

- Extreme water levels at 50m from shoreline can serve as a proxy for wave runup.

Abstract

Boussinesq modeling of wave transformation over coral reefs to date focuses mainly on wave dynamics at the laboratory scale using idealized fringing reef profiles with relatively smooth surfaces. To better understand the cross-shore wave dynamics associated with coastal wave run-up in field studies of fringing reefs, a numerical study

based on the one-dimensional horizontal (1DH) weakly dispersive, highly nonlinear Boussinesq equations is carried out for two realistic fringing reefs with different reef configurations and roughness characteristics in the Republic of the Marshall Islands. A series of incident wave events are tested and compared to the field observations. The numerical simulations demonstrate that the adopted model reproduces the cross-shore sea and swell (SS) waves, infragravity (IG) waves and wave-induced setup over the rough reef flats, which are the components of wave-driven runup and coastal inundation. The model then is applied to investigate the mechanisms of IG wave generation and normal mode excitation on the reef flat. Finally, the shoreline response of waves to the variations of the surf zone seabed profile and the phase of incident waves is examined via the numerical simulations. The ability to predict shoreline runup based on nearshore pressure measurements also is considered.

⟨ Previous   Next ⟩

Keywords

Wave transformation; Boussinesq equations; Fringing reef; Infragravity waves

---

1. Introduction

Low-lying atoll islands with fringing coral reefs are especially vulnerable to wave-driven inundation during extreme wave events [1], [2], [3]. Hence, the accurate prediction of the nearshore waves is important to assess the role of fringing reefs in mitigating coastal flooding events. Corals commonly grow to mean low tidal levels and may impose a shallow water control on the waves reaching reef flats. Ocean waves first shoal on the fore-reef slope and then break near the reef edge. The surf-zone processes typically extend over a certain distance on the outer reef flat, and generate a setup of the mean water level, a phenomenon first described by Munk and Sargent [4]. Meanwhile, a majority of energy within the Sea and Swell (SS) frequency band (between 0.04 and 0.4Hz) is dissipated in the surf zone [e.g., [5], [6], [7]]. Additional SS energy may be dissipated by bottom friction and/or turbulent bore dissipation during wave transformation over the reef flat [e.g., 8]. The shoreline wave run-up and overwash frequently are found to be dominated by wave energy within the infragravity (IG) frequency band (between 0.001 and 0.04Hz) [e.g., [9], [10]]. Both field observations [e.g., 9,[11], [12]] and laboratory experiments [e.g., [13], [14]] also have reported that under higher wave levels, the IG energy level could be further amplified due to the excitation of reef-flat normal modes.

Over recent decades, numerical models have become efficient tools to investigate the coral reef hydrodynamics associated with waves. Modeling wave processes over realistic coral reefs poses several challenges such as a steep fore-reef slope, complex reef morphology and spatially-varying surface roughness. Also, the process of wave transformation typically needs to be modeled for long-time scales (several hundred waves) and a large spatial scale (over the entire reef profile). Coral reef hydrodynamics in field environments previously have been modeled using 2DH and 3D nonlinear shallow water equations based models or non-hydrostatic models to study both the waves and the mean flows, and typically the radiation stress concept [15] is used to couple the waves and the flows [e.g., [16], [17], [18], [19], [20], [21], [22], [23]]. The variations of reef morphology and ocean forcing have been well considered in such models. However, the wave modules in those coupled models are frequently phase-averaged and individual wave motions over the reefs are not captured.

The interaction between waves and reef profiles at the laboratory scale have been extensively studied by many researchers with nonlinear spectral models [e.g., 24], non-hydrostatic models [e.g., 25] and Navier-Stokes equations

based models [e.g., 26] in the past decade. Among various approaches, the computationally efficient and phased-resolving model based on the Boussinesq equations often is used. This depth-integrated modeling approach employs a polynomial approximation to the vertical profile of <u>velocity field</u>, thereby reducing the dimensions of a three-dimensional problem by one. It is able to account for both nonlinear and dispersive effects for intermediate water levels. Boussinesq models combined with empirical treatments of wave breaking and bottom friction can well simulate the motions of regular waves [27], [28], [29], irregular waves [13], [29], [30], [31], <u>solitary waves</u> [32], [33], [34] and infragravity waves [35], [36] over laboratory fringing reef profiles. However, field applications of Boussinesq models have received less attention in the literature. Roeber and Cheung [33] applied the 2DH form of the Boussinesq model from Roeber et al. [32] to a field site at Hawaii, and the transformation of irregular incident waves, wave-induced setup and development of sub and super-harmonics were reproduced. Their grid size, however, was relatively coarse (3 m) and the computation was restricted to a small region (440×560 grid cells). Shimozono et al. [37] implemented a Boussinesq model to assess the components contributing to field measurements of extreme run-up at Eastern Samar by super typhoon Haiyan. They, however, only used the 1DH form of the model to simulate the wave evolution over cross-shore reef topographies with varying reef widths and beach slopes. Nevertheless, both studies mentioned above have shown the potential of Boussinesq-type models to replicate the field observations of wave processes over fringing reefs.

In recent years, wave-driven coastal inundation at reef-fringed shorelines of low-lying atolls in the Republic of the Marshall Islands (RMI) has received considerable attention among scholars. Becker et al. [38] reported a six-month cross-shore observation of waves and water level collected at two fringing reef atolls. They found that the tidally varying setup was due to the combined effects of depth-limited wave heights on the reef flat, and the tidally dependent breaking on the fore-reef slope. Subsequently, Merrifield et al. [2] used the 2% exceedance water level at the nearest shoreline sensor to assess wave-driven extreme water-levels leading to inundation events at the RMI field sites. More recently, via an Empirical Orthogonal Function (EOF) analysis, Becker et al. [11] suggested that the dominant low-frequency variability during energetic wave events on these two reef flats were modal. They also conducted cross-covariance analysis indicating that the normal modes were excited by the breakpoint forcing mechanism. Among these studies, several concerns have been raised due to limitations of the field observations. For example, the <u>bathymetry</u> in the surf zone could not be measured due to the turbulence and air entrainment. The measured incident waves on the fore-reef slope over the entire sampling period may not be fully representative of local wave conditions. The shoreline runup was not measured with the instrument array, in part due to the presence of irregular shore protection structures.

Therefore, to address the above limitations, we carry out a <u>numerical modeling</u> study by employing a weakly dispersive and fully nonlinear depth-integrated Boussinesq-type model [39]. The 1DH form of the model has been applied successfully by Yao et al. [28] for wave transformation over an idealized laboratory reef and by Yao et al. [30] over a field reef flat with an <u>excavation pit</u>. In this study, we first show the robustness of the 1DH model to reproduce the cross-shore wave processes, including SS waves, IG waves and breaking-wave setup, which are the main components of wave-driven shoreline water levels for a fringing reef [2]. The model then is used to analyze the mechanisms of IG wave generation on the reef flat and modal excitation over the reef flat. Finally, the model runs address the following questions: (1) how is the shoreline wave response affected by the morphological uncertainty in the surf zone? (2) how is the shoreline wave response affected by the phasing of incident waves? (3) is a water level measurement made near the shoreline representative of shoreline run-up?. We remark that although recent studies have shown some improvements on different aspects of the Boussinesq models such as dispersion properties [e.g., 40,41,43], wave breaking treatment [e.g., 42] and bottom friction simulation [e.g., 43], the focus of the present study is to validate and apply an widely used Boussinesq model in field reef environments rather than to seek any improvement on the adopted model.

The remainder of this paper is organized as follows. In Section 2, the mathematical formulation, numerical scheme, boundary/initial conditions and energy dissipation sub-models are described. In Section 3, numerical simulations are conducted under a series of representative wave events to show the robustness of the model. Model applications are reported in Section 4, and the main conclusions drawn from this study are given in Section 5.

2. Description of the numerical model

2.1. Governing equations

Let the x-coordinate point in the direction of wave propagation and the z-coordinate point upward with its origin at the still water level, and t denotes the time. The 1DH Boussinesq-type continuity and momentum equations in conservative form are expressed as

$$\frac{\partial H}{\partial t} + \frac{\partial H u_\alpha}{\partial x} + D^c = 0 \tag{1}$$

$$\frac{\partial H u_\alpha}{\partial t} + \frac{\partial H u_\alpha^2}{\partial x} + gH\frac{\partial \eta}{\partial x} + gHD^x + u_\alpha D^c + R_f - R_b = 0 \tag{2}$$

where the streamwise horizontal velocity $u_\alpha\,[x,\ z = z_\alpha\,(x,t)]$ is evaluated at $z_\alpha\,(x,t) = 0.531h$ [44], $H = h + \eta$ is the total instantaneous water depth, h is the still water depth, η is the water surface elevation, g is the gravity acceleration, D^c and D^x are the second-order terms, see Appendix A for details. R_b and R_f are ad-hoc dissipative terms accounting for the wave breaking and the bottom friction, respectively. Sub-models for R_f and R_b will be introduced below.

2.2. Numerical scheme

A third-order Adams–Bashforth predictor and a fourth-order Adams–Moulton corrector scheme are used for time marching. A shock-capturing finite-volume-based approach is used for the spatial discretization. The leading-order terms are solved with the fourth-order MUSCL-TVD (monotone upstream-centered scheme for conservation laws-total variation diminishing) scheme, while a cell-average finite-volume method is implemented for the second-order terms. Compared to the traditional finite-difference-based methods, finite-volume formulations in conservative form are generally more stable and accurate. The numerical scheme is accurate to $O(\Delta t^4)$ in time and $O(\Delta x^4)$ or $O(\Delta x^2 \mu^2)$ in space, where μ is the wavelength scaling parameter defined as $\mu = h/L$, and L is the incident wave length. For more details about the solver, see Kim et al. [45].

2.3. Sub-models of wave breaking and bottom friction

It is well known that the depth-integrated Boussinesq equations cannot describe the overturning of a free surface and the detailed wave breaking process. Hence, several techniques have been proposed in the literature for modeling wave breaking in the surf zone. One example is a hybrid model in which wave breaking is modeled by locally switching the Boussinesq equations to the nonlinear shallow water equations when the Froude number exceeds a certain threshold [e.g., 46,47]. Another common approach is to add an ad-hoc dissipation term to the momentum equation. This approach requires an energy dissipation mechanism and a trigger mechanism to initiate the wave breaking. In this study, the eddy-viscosity-type formulation proposed by Kennedy et al. [48] is used to model the wave energy dissipation caused by breaking waves. The expression for R_b in Eq.(2) is given by

$$R_b = [\nu(H u_\alpha)_x]_x \tag{3}$$

where v is an empirical <u>eddy viscosity</u> given by the following zero-equation <u>turbulence model</u>

$$\nu = B\delta H \eta_t \tag{4}$$

where δ is an empirical coefficient to correct both the mixing-length and friction-velocity scales. It is an essential parameter for turbulence energy dissipation, and can be obtained by calibrating the simulations with the measurements. The parameter B accounts for the trigger mechanism to ensure a smooth transition between the breaking and the non-breaking states, which gives

$$B = \begin{cases} 1 & \eta_t \geq 2\eta_t^* \\ \eta_t/\eta_t^* - 1 & \eta_t^* < \eta_t < 2\eta_t^* \\ 0 & \eta_t \leq \eta_t^* \end{cases} \tag{5}$$

where η_t^* determines the onset and stoppage of the breaking process, and it is evaluated by

$$\eta_t^* = \begin{cases} \eta_t^{(F)} & t - t_0 \geq T^* \\ \eta_t^{(I)} + \frac{t-t_0}{T^*}\left(\eta_t^{(F)} - \eta_t^{(I)}\right) & 0 \leq t - t_0 < T^* \end{cases} \tag{6}$$

where $\eta_t^{(I)}$ is a threshold value at the breaking inception, $\eta_t^{(F)}$ is a saturated value for the breaking cessation, t_0 is the time at which the breaking event starts, $t - t_0$ is the age of breaking event, T^* is the duration of the breaking event. For the trigger-related parameters in Eq.(6), the following expressions suggested by Lynett and Liu [39] are used in the model

$$\eta_t^{(I)} = \alpha_1 \sqrt{gH}; \eta_t^{(F)} = \alpha_2 \sqrt{gH}; T^* = \alpha_3 \sqrt{H/g} \tag{7}$$

where $\alpha_1, \alpha_2, \alpha_3$ are also empirical parameters that need to be calibrated. The bottom friction R_f in Eq.(2) is calculated by the Manning frictional law

$$R_f = \frac{gn^2}{H^{1/3}}|u|\,u \tag{8}$$

where values of the Manning coefficient (n) ranging from 0.01 to 0.1 may be found in the literature [49] for commonly used surface materials. We remark that vegetation effect and seepage velocity inside the coral colonies (in analogy to the porous medium) are not considered in above formulations.

2.4. Boundary and initial conditions

The internal source method using a distributed source function in the <u>continuity equation</u> as proposed by Wei et al. [50] is adopted in this study for the numerical wave generation. The radiation (or open) boundary condition is used at the offshore boundary accompanied by a sponge layer to damp the energy of outgoing waves. The sponge layer is applied in a manner similar to that recommended by Kirby et al. [51]. The extrapolating moving boundary algorithm proposed by Lynett et al. [52] is used to describe the wave run-up and run-down processes around the coastline. The initial condition assumes no motion of waves or currents in the computational domain.

3. Model validation

3.1. Description of the field measurements

Two field experiments as reported by Becker et al. [38] are revisited in this study (Fig. 1). One of the field sites was on Majuro atoll in the western tropical Pacific. A cross-shore sensor array was deployed on the <u>fringing reef</u> adjacent to the College of the Marshall Islands (denoted as CMI) on the east side of the atoll. The CMI reef flat is

approximately 250 m wide, 0.8 m deep. The second site was on Roi-Namur (denoted as ROI) at the northern tip of the Kwajalein Atoll, approximately 400 km northwest of Majuro. The cross-shore sensor array was deployed across the approximately 350 m wide, 0.8 m deep, fringing reef flat. The detailed reef sites and the instrument locations were described in Merrifield et al. [2], see their Fig. 1. The offshore bathymetry at each reef site was obtained from diver surveys; however, the turbulence in the water column prevented mapping the profile through the surf zone. As a result, the bathymetry was linearly interpolated between the shallowest diver depth measurement and the estimated edge of the reef flat from satellite images. The tides at both reefs were mixed semidiurnal and diurnal with a mean range of 1 m and a typical spring range of 1.6 m. The reef flats were completely submerged at the mean higher water level during the course of experiments.
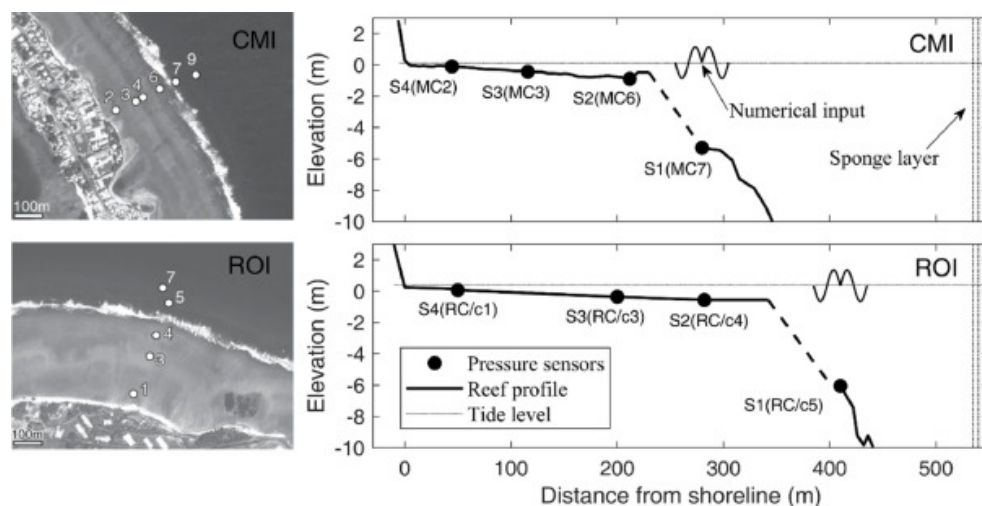
Download: Download high-res image (373KB)
Download: Download full-size image

Fig. 1. Left: Satellite images showing the surveyed cross-reef transects at CMI reef (upper panel) and ROI reef (lower panel); Right: the numerical settings of CMI reef (upper panel) and ROI reef (lower panel); Dashed line indicates the surf zone bathymetry obtained by linear interpolation.

In this study, we consider the wave and water level recorders with pressure measurements from sensors 2 to 7 at CMI, denoted as MC2 to MC7, and sensors 1 to 5 at ROI, denoted as RC1 to RC5 (Fig. 1). All data were collected at 1 Hz sample frequency over 1.5 h bursts sampled every 3 h. Burst samples are not included in the analysis when water level over a sensor is less than 0.1 m. SS surface elevations are estimated from detided bottom pressure measurements using linear wave theory. Wave setup is computed from the 30 min average water depths. Significant wave heights were computed over 30 min intervals as 4 times the standard deviation of the band-passed wave bursts. The SS significant wave height at the fore-reef slope ranged from 1 to 2.5 m, with slightly higher values at ROI than at CMI due to wave refraction around the atolls. Peak wave periods are between 6 and 24 s at CMI and 4 to 21 s at ROI with arrivals primarily from the northeast. Near normal incidence was found at the fore-reef sensors for both sites. More detailed descriptions of the two experiments are given in Becker et al. [38].

3.2. Numerical settings

Referring to the 1DH computational domain (Fig. 1), the location of instruments and the morphology of reefs are designed to reproduce the main aspects of the field conditions. The reef profiles closely follow those in Becker et al. [38], including the linearly interpolated regions on the fore-reef slopes. Four sensor locations (S1~S4) across each reef profile are selected, representing the locations on the fore-reef slope S1 (i.e., MC7 for CMI and RC5 for ROI), near the reef crest S2 (i.e., MC6 for CMI and RC4 for ROI), at the mid-reef flat S3 (i.e., MC3 for CMI and RC3 for ROI),

and near the shoreline S4 (i.e., MC2 for CMI and RC1 for ROI), respectively. On the offshore side, the fore-reef slope is truncated and replaced by a flat bottom at the water depth of 10m. Incident waves are generated using the direct measurement of the time-series of free surface elevations at the fore-reef slope (S1), and the initial still water level is set as the mean sea level modulated by the tide. Since the water depth at the wave generation point S1 is not very large, we only solve the one-layer model whose linear dispersion accuracy is near $kh = 3$, and k is the wave number [39]. A dissipative sponge layer, typically of a width of 1.25 times the incident (peak) wave length, is placed at the offshore boundary to ensure that the outgoing waves are absorbed satisfactorily. For the shoreward boundary, a "solid wall" is placed behind the back-reef beach to prevent water overtopping over the beach. Numerical wave gauges are placed at the same cross-shore positions as their counterparts in the field experiments. The initial condition assumes no wave or current motion in the computational domain thus the initial 100 wave cycles are not used in the subsequent data analysis to remove the transient effect. A grid size of approximately 0.25m with a Courant number of 0.2 is generally found to be sufficient to discretize the computational domain and maintain the numerical stability in this study. No significant differences in terms of wave processes across the reef can be observed with further refinement of the grid. Finally, a 4-point filter based on the moving average method is used to reduce the curvature of the rapidly varying bathymetry, especially around the toe of fore-reef slope and the outer reef edge due to the derivatives of the water depth that are included in the higher order terms of the Boussinesq equations.

A series of 1.5-h incident wave events are simulated for both CMI (7 events) reef and ROI (6 events) reefs, representing a variety of wave and tidal conditions, see Table 1. We then divide the 1.5-h record into 3 bins with each bin of 30min. Total, SS and IG wave heights are estimated as four times the standard deviation of the simulated free surface elevation spectrum integrated within the total band (0.001–0.4Hz), the SS band (0.04–0.4Hz) and the IG band (0.001–0.04Hz), respectively. The mean water level across the reef is obtained by time-averaging the computed free surface elevations among the sampling locations.

Table 1. Wave and tide conditions for a series of selected 1.5-hour wave events.

Event I.D.	H_s (m)*	T_p (s) *	Tidal level (m)	Event I.D.	H_s (m)*	T_p (s) *	Tidal level (m)
CMI44	1.68	14.59	0.28	ROI51	2.55	15.84	0.41
CMI69	1.79	14.14	0.53	ROI345	2.05	15.30	0.74
CMI313	1.72	13.85	0.74	ROI481	2.37	15.79	0.69
CMI851	1.86	14.88	−0.19	ROI486	2.30	15.04	0.56
CMI852	1.86	15.61	0.16	ROI777	2.34	15.00	0.16
CMI853	2.00	15.98	0.12	ROI783	2.31	13.92	−0.06
CMI864	1.99	15.30	0.34				

*
    Total significant wave height (H_s) and peak wave period (T_p) at S1 on the fore-reef slope.

Our previous sensitivity analysis [53] has shown that the simulated waves are much more sensitive to the bottom friction coefficient than the wave breaking related parameters. Thus for the sub-model of wave breaking in Section 2.3, the following set of empirical parameters as suggested by Lynett and Liu [39] for plane beaches is chosen for Eqs.(4) and (7): $\delta = 6.0, \alpha_1 = 0.65, \alpha_2 = 0.08, \alpha_3 = 8$. These values also have been validated by a field fringing reef profile with an excavation pit [30]. As reported by Becker et al. [38], the corals at both CMI and ROI

reefs have a variety of species and they are unevenly distributed on the fore-reef slope and the reef flat. However, for simplicity, we assume a uniform friction coefficient along the reef profile in this study. The Manning coefficients are obtained by calibrating the model predictions against the measurements in view of the SS waves, IG waves, and wave setup at the four locations (S1–S4) for all events given in Table 1. The model skill value is adopted to evaluate the performance of the model [54], which gives

$$skill = 1 - \frac{\sum |X_{\mathrm{mod\ el}} - X_{obs}|^2}{\sum (|X_{\mathrm{mod\ el}} - \overline{X_{obs}}| + |X_{obs} - \overline{X_{obs}}|)^2} \tag{9}$$

where $X_{\mathrm{mod\ el}}$ is the predicted value, X_{obs} is the measured value. The overbar indicates that the average value is taken. For a perfect model result, the value of the skill would approach 1, whereas it would be close to 0 for an obvious predictive error. The Manning frictional coefficient is obtained by fitting the combined simulated SS wave heights, IG wave heights and mean water levels to the field observations with global optimal skill values achieved at the field sampling locations. Consequently, it is possible that the individual skill value for SS wave heights, IG wave heights or mean water levels at a specific location may not be high. After a sensitivity analysis (see Section 3.6), the best-fit Manning coefficients $n = 0.015$ and $n = 0.012$ are obtained for CMI and ROI reefs, respectively. These values are consistent with the observation that CMI reef has the denser fore-reef coral coverage than the ROI reef [38], and they are larger than $n = 0.01$ obtained for a laboratory smooth reef surface [28].

3.3. Cross-shore variations of SS waves, IG waves and mean water levels

Observed and predicted SS and IG significant wave heights for each bin of data are compared in Fig. 2, Fig. 3, respectively, for the two reef sites. Wave breaking generally occurs around the reef crest thus the SS wave height (H_{SS}) decreases from S1 to S2. The incident SS wave energy at S1 is reduced by up to 80% as the SS waves approach the shoreline (S4). For the IG frequency band, the IG wave height (H_{IG}) on the fore-reef slope (S1) is due to the presence of shoaling bound waves [55] and it is relatively small. However, some wave energy within the IG band is generated in the surf zone around S2 due to the breakpoint forcing as discussed in Section 4.1. After that, H_{IG} increases from the reef crest (S2) to the shoreline (S4) because of the excitation of normal modes on the reef flat (see also Section 4.1). Near the shoreline (S4), H_{IG} is found to be larger than the H_{SS} at both reef sites.
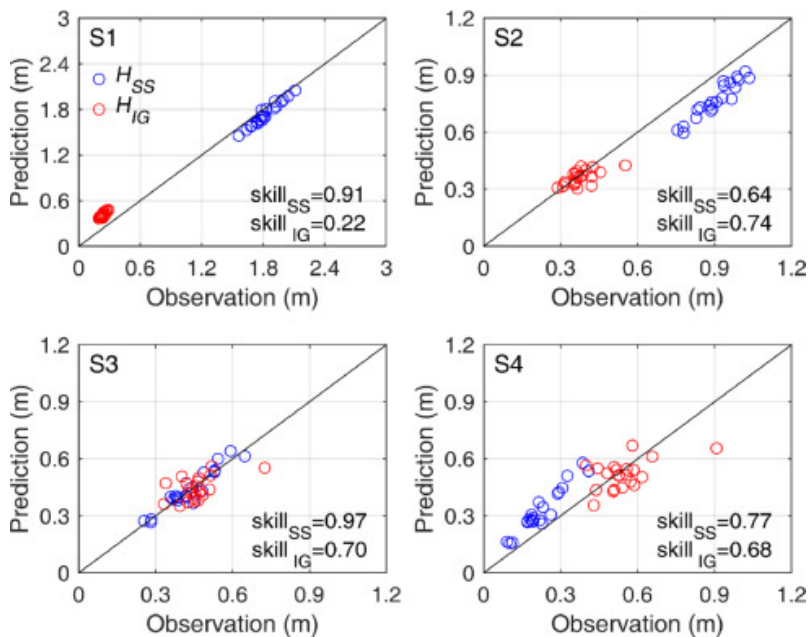
Download: Download high-res image (412KB)

Download: Download full-size image

Fig. 2. Predicted vs. observed significant wave heights at the four sampling locations (S1~S4) for all CMI event bins. H_{SS}- SS wave height, H_{IG}- IG wave height.
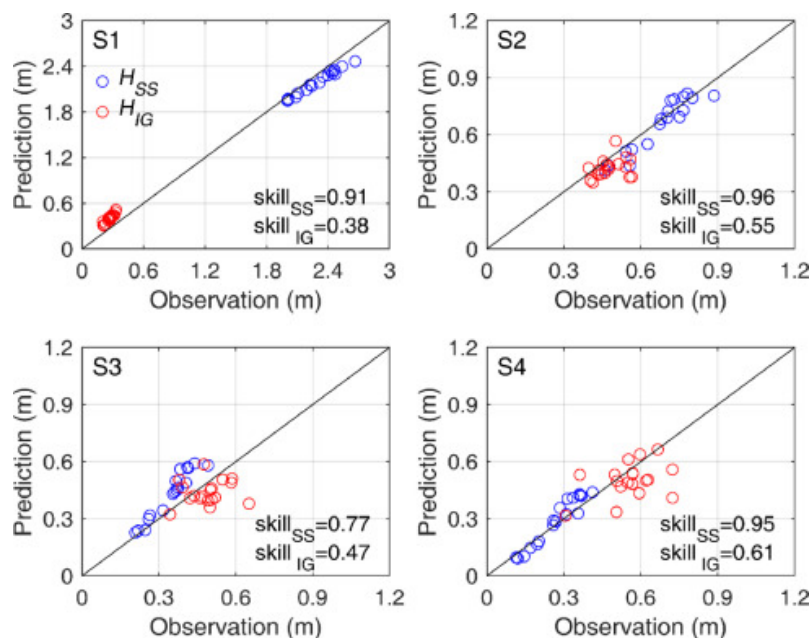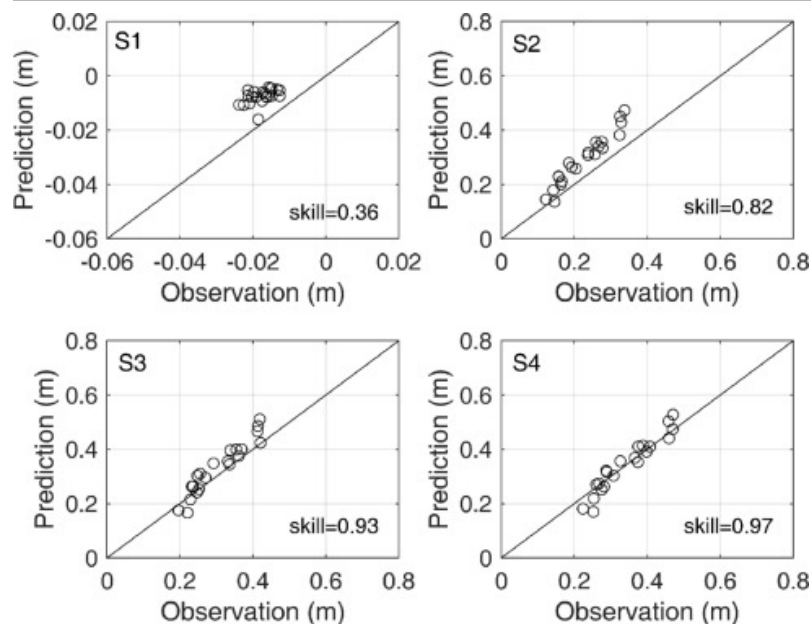

Download: Download high-res image (420KB)

Download: Download full-size image

Fig. 3. The same as Fig.2 but for all ROI event bins.

Generally, the simulations agree reasonably well with the measurements with the skill values for SS and IG waves at most of the sampling locations larger than 0.6, indicating the robustness of the adopted model. On the fore-reef slope (S1) where incident waves are generated, H_{SS} is well predicted for both reefs, while a slight over-prediction occurs for H_{IG}. This may be due to the fact that the sponge layer at the offshore boundary in Fig.1 could not effectively absorb the reflected long waves thus a partial-standing wave pattern may exist seaward of S1. Near the reef crest (S2), H_{SS} agrees well at ROI, but it is consistently under-predicted at CMI, whereas H_{IG} is reasonably reproduced at both sites. This may be due to the fact that a uniform roughness is assumed in the model that oversimplifies the variable reef roughness on the fore-reef slope for the field studies. Such roughness uncertainty appears to have more effect on the SS waves at CMI because it has the denser fore-reef coral coverage than the reef at ROI as previously mentioned. From the mid-reef flat (S3) to the shoreline (S4) at the two reefs, the agreement of H_{SS} and H_{IG} between predictions and measurements are less satisfactory, particularly for S4 at CMI reef and S3 at ROI reef, where larger data scatter is observed. A potential reason for the increased scatter again may be due to the assumed uniform roughness on the reef flat in the model.

We next compare the predicted and the observed mean water levels at the four sampling locations for the reefs at CMI (Fig.4) and RMI (Fig.5). On the fore-reef slope prior to wave breaking (S1), wave setdown due to shoaling is over-predicted with relatively low skill values for both reefs. This is expected due to the requirement on the conservation of mass for our closed numerical domain: the wave setup over the reef flat must be balanced by the setdown in the rest of the domain, such as at S1, but field environments do not have this requirement. Starting from the reef crest (S2) where the surf zone processes occur, wave setup is generated and the model predictions are consistent with the observations, particularly for ROI. Wave setup is found to be almost constant from the mid-reef flat (S3) to the shoreline (S4) after waves have ceased breaking, and their values are well captured by the model for both reefs.

Fig. 4. Predicted vs. observed mean water level at the four sampling locations (S1–S4) for all CMI event bins.
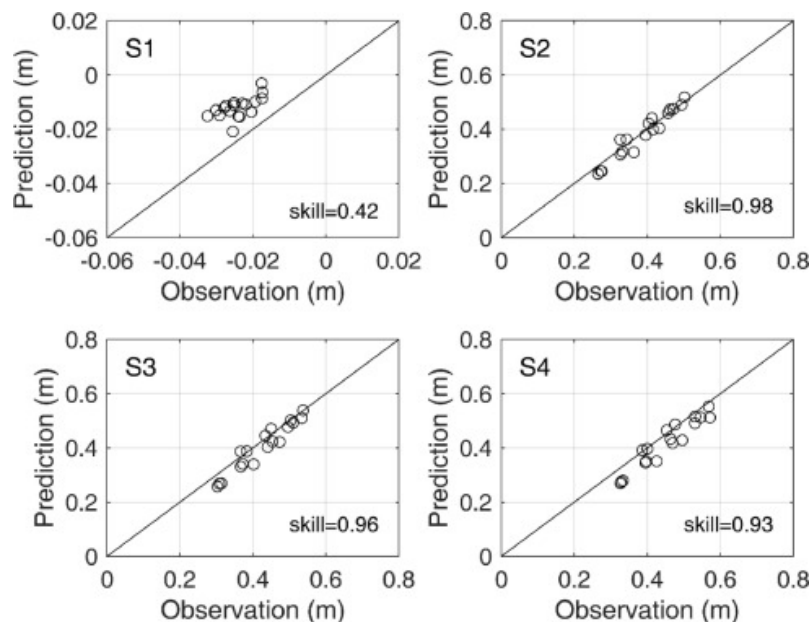
Fig. 5. The same as Fig.4 but for all ROI event bins.

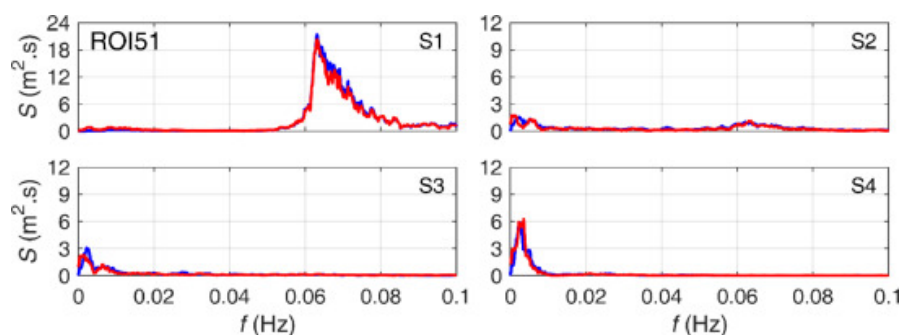## 3.4. Cross-shore evolution of wave spectra

In this section, two typical wave events, designated as CMI853 and ROI51, are reported in Fig. 6, Fig. 7 for the two reefs, respectively. Wave spectra are obtained by Fast Fourier transforming a 1.5-h record smoothed over 10 adjacent frequency bands.
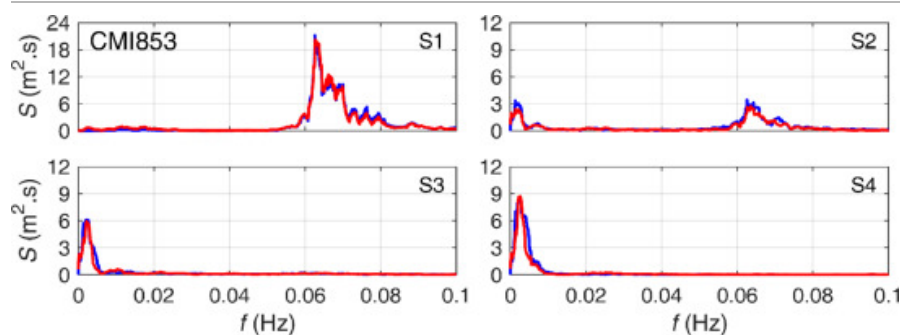
Download: Download high-res image (221KB)

Download: Download full-size image

Fig. 6. Wave spectra at the four sampling locations (S1~S4) for the CMI853 event. Red lines –predictions, blue lines –observations.
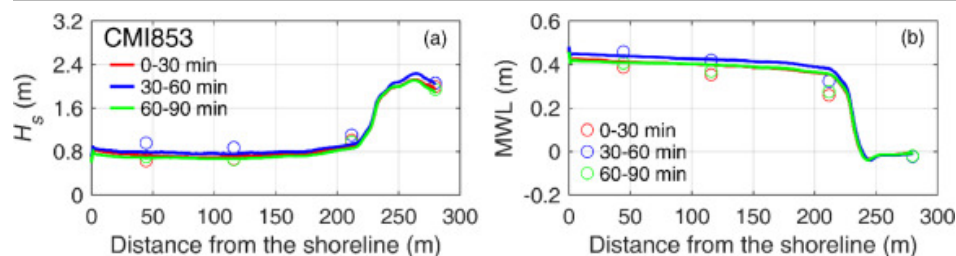

Download: Download high-res image (220KB)

Download: Download full-size image

Fig. 7. The same as Fig.6 but for the ROI51 event.

Overall, the numerical model satisfactorily reproduces the cross-shore evolution of wave spectra. Near the reef crest (S2) or mid-reef flat (S3), some differences within the IG band exist between the computed and the observed spectra. We again attribute this mismatch to the uneven bottom roughness in field environments, which may be not accurately captured in our model. When examining the variation of cross-shore wave spectra, we find that although most of the surf zone processes occur on the fore-reef seaward of the reef crest (S2), a considerable amount of SS energy around the peak frequency still exists, particularly for the reef at CMI. As the SS waves propagate further shoreward, they experience additional dissipation by friction on the reef flat, thus the remaining SS energy around the peak frequency is very small near the shoreline (S4). In contrast, the IG energy increases shoreward from the reef crest (S2) to the shoreline S4 for both reefs, providing a dominant contribution to the shoreline wave energy at both reefs.

## 3.5. Cross-shore evolution of wave height and mean water level

The cross-shore evolution of total significant wave height (H_s) and mean water level (MWL) also are computed for each bin at the four sampling locations (S1~S4), and they are compared with the observations in Fig. 8, Fig. 9, respectively, for the two events.

Fig. 8. Cross-shore distribution of total significant wave height (H_s) and mean water level (MWL) for the CMI853 event bins. Solid lines - predictions, Circles - observations from S1~S4.
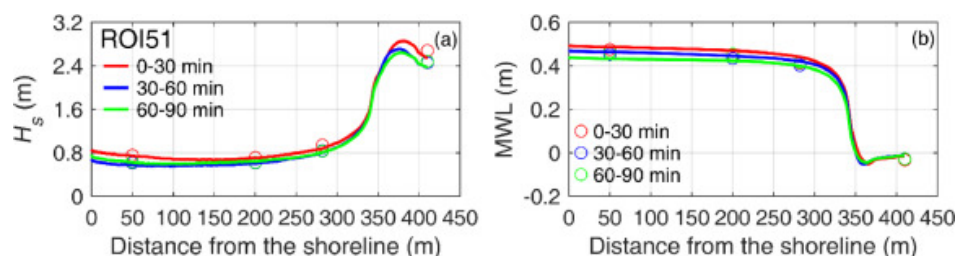
Fig. 9. The same as Fig.8 but for the ROI51 event bins.

Overall, the simulated H_s and MWL are in reasonable agreement with the measurements at the four locations for almost all bins. When incident waves transform over the two reefs, waves first shoal on the fore-reef slope (S1) and then break, thus an increase of H_s and a corresponding decrease of mean water level (wave setdown) is observed near S1. After wave breaking occurs, H_s decreases rapidly in the surf zone, resulting in an increase of MWL (wave setup). At the mid-reef flat (S3) and near the shoreline (S4) shoreward of the surf zone, H_s becomes more or less constant, due to a decrease of wave energy within the SS band compensated by an increase of energy within the IG band as indicated in Figs.6 and 7. Also no notable variation of wave setup from S3 to S4 could be found. This is due to the slow attenuation of the waves by the bottom friction as they propagate over the reef flat. Further, there are no rip channels near the surveyed cross-shore transects at two reef sites, thus the effect of current (both cross-shore and alongshore) on the wave setup appears to be negligible.

3.6. Model sensitivity to the reef roughness coefficient

Finally, an analysis of the sensitivity of the simulated SS wave height (H_{SS}), IG wave height (H_{IG}) and mean water level (MWL) at the four sampling locations (S1~S4) to the Manning frictional coefficient is conducted based on the event bins selected for both reefs. The tested Manning frictional coefficient (n) in this analysis ranges from 0.009 to 0.021 for the CMI reef and 0.006 to 0.018 for the ROI reef, respectively. The model's performance is evaluated using the skill values computed from Eq.(9), which are shown in Tables 2 and 3 for the two reefs, respectively.

Table 2. Skill values of simulated SS wave height (H_{SS}), IG wave height (H_{IG}) and mean water level (MWL) at the four sampling locations (S1~S4) with different Manning coefficient n for all CMI event bins.

Skill Value	S1	S2	S3	S4
	(H_{SS}, H_{IG}, MWL)	(H_{SS}, H_{IG} MWL)	(H_{SS}, H_{IG} MWL)	(H_{SS}, H_{IG}, MWL)
n=0.009	(0.91, 0.20, 0.34)	(0.66, 0.64, 0.84)	(0.95, 0.59, 0.95)	(0.70, 0.59, 0.97)
n=0.012	(0.91, 0.21, 0.36)	(0.64, 0.65, 0.82)	(0.97, 0.54, 0.94)	(0.75, 0.54, 0.96)
n=0.015	(0.91, 0.22, 0.36)	(0.64, 0.74, 0.82)	(0.97, 0.70, 0.93)	(0.77, 0.68, 0.97)
n=0.018	(0.92, 0.23, 0.39)	(0.59, 0.50, 0.79)	(0.96, 0.39, 0.92)	(0.85, 0.40, 0.96)
n=0.021	(0.91, 0.23, 0.40)	(0.57, 0.47, 0.77)	(0.94, 0.36, 0.91)	(0.89, 0.36, 0.96)

Table 3. The same as Table 2 but for all ROI event bins.

| Skill Value	S1	S2	S3	S4
	(H_{SS}, H_{IG}, MWL)	(H_{SS}, H_{IG}, MWL)	(H_{SS}, H_{IG}, MWL)	(H_{SS}, H_{IG}, MWL)
n=0.006	(0.87, 0.37, 0.42)	(0.94, 0.77, 0.96)	(0.71, 0.65, 0.93)	(0.91, 0.70 0.91)
n=0.009	(0.88 0.37, 0.41)	(0.94, 0.68, 0.97)	(0.72, 0.62, 0.94)	(0.92, 0.67, 0.91)
n=0.012	(0.91, 0.38, 0.42)	(0.96, 0.55, 0.98)	(0.77, 0.47, 0.96)	(0.95, 0.61, 0.93)
n=0.015	(0.91, 0.39, 0.42)	(0.95, 0.51, 0.98)	(0.82, 0.40, 0.96)	(0.96, 0.52, 0.94)
n=0.018	(0.91, 0.40, 0.41)	(0.94, 0.47, 0.98)	(0.86, 0.31, 0.96)	(0.97, 0.46, 0.94)

For both reefs, it is anticipated that varying n will have little effect on the skill values at the fore-reef location (S1) as S1 is the location of the numerical input. From S2 to S3 on the reef flat, skill values of H_{SS} and H_{IG} are generally much more sensitive to n than those for the MWL. For the CMI reef, the highest skill values are found at $n = 0.015$, expect for those of H_{SS} at S2 and S4, where the maximum values appear at $n = 0.009$ and $n = 0.021$, respectively. Consequently, we choose the intermediate value, $n = 0.015$ as the best choice for the Manning coefficient in the subsequent simulations for the CMI reef. For the ROI reef, skill values of H_{SS} generally increase with increasing n whereas those for H_{IG} decrease with increasing n. Considering these competing effects, we adopt $n = 0.012$ for the ROI reef. We remark that using a spatially varying value of n may further improve the model predictions but this would require observations of the patterns of reef roughness at the two field sites that currently are unavailable.

4. Model applications

4.1. IG wave generation and its modal response near the shoreline

A cross-covariance analysis of the field measurements [11] suggests that the IG waves on the reef flat at the two reefs are generated by the time variation of the breakpoint (i.e., the breakpoint forcing mechanism). The envelope of the SS wave group from the fore-reef wave measurements was employed as the indictor of the breakpoint forcing. In this study, we obtain the temporal variation of the incipient breakpoint locations (Figs. 10a and 11a) where the breaking model is triggered in the numerical simulations for both 1.5-hour events of CMI853 and ROI51. It appears that their spectra (Figs. 10b and 11b) are commensurate with the spectra (Figs. 10c and 11c) of the envelope (obtained by a Hilbert transform) of timeseries free surface elevations at S1 on the fore-reef slope prior to wave breaking, confirming that the use of SS wave group envelope as a proxy for the breakpoint oscillation is

appropriate in previous field studies [e.g., [9], [10], [11]]. We then follow Péquignet et al. [9] to compute the spectral coherence (indicating the cross-correlation) between the envelope at S1 and the wave timeseries near the shoreline (S4) based on our simulations. High coherence values around 0.9 could be found for both events (Figs. 10e and 11e), suggesting that the IG oscillations near the shoreline are driven by the modulation of incident short wave groups.
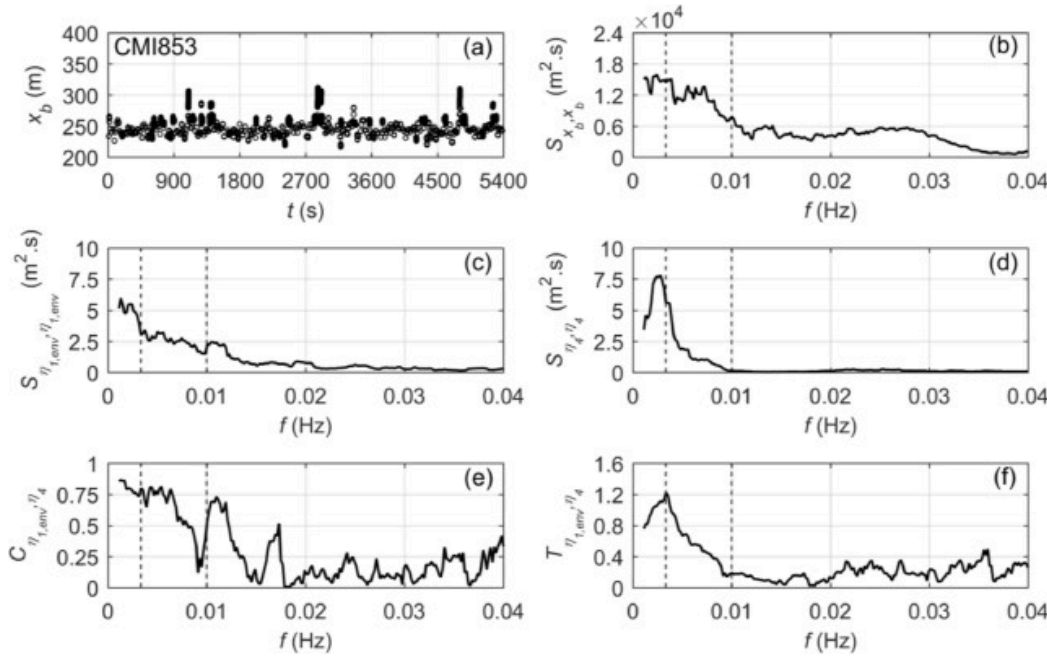
Fig. 10. (a) Temporal variation of cross-shore breakpoint location (x_b) with $x_b = 0$ at the shoreline for the CMI853 event; (b) Auto-spectrum of x_b within the IG band for the CMI853 event; (c) Auto-spectrum of the envelope of free surface elevation at S1 on the fore-reef slope ($\eta_{1, env}$) within the IG band for the CMI853 event; (d) Auto-spectrum of the free surface elevation at S4 near the shoreline (η_4) within the IG band for the CMI853 event; (e) Spectral coherence between η_4 and $\eta_{1, env}$ for the CMI853 event; (f) Transfer function between η_4 and $\eta_{1, env}$ for the CMI853 event. The vertical dotted lines denote the first two theoretical resonant frequencies, respectively.
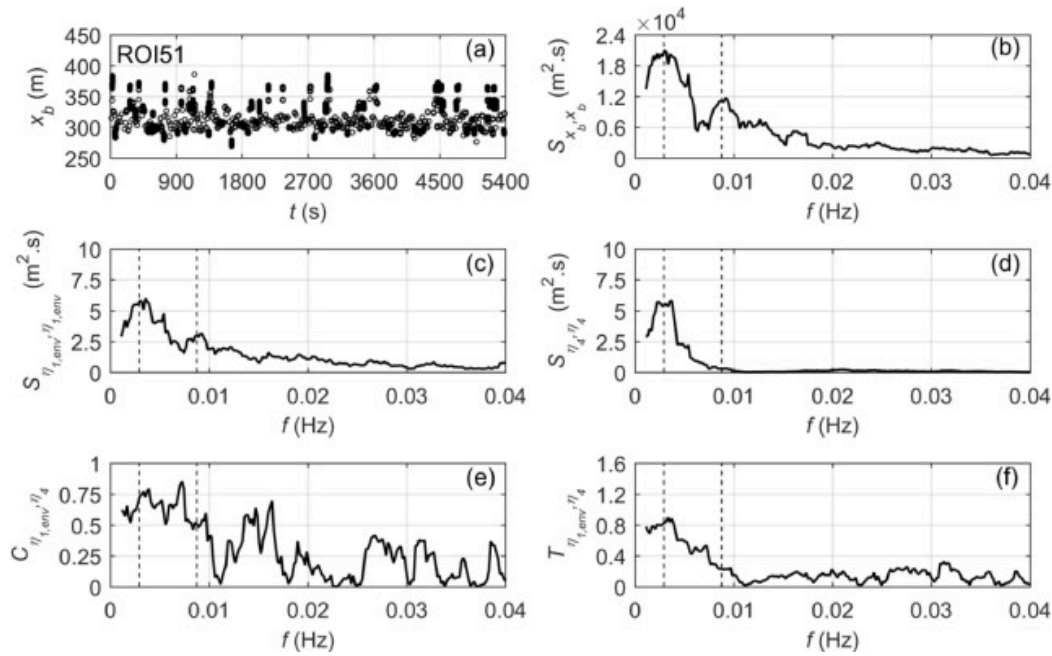
Fig. 11. The same as Fig. 10 but for the ROI51 event.

A fringing reef profile generally has been regarded as a semi-enclosed basin that supports normal modes of oscillations [e.g., 2,9,13]. The resonant periods for an idealized step reef, are given by

$$T_n = \frac{4W}{(2n+1)\sqrt{gd}} \quad n = 0, 1, 2 \ldots \tag{10}$$

where W is the cross-shore reef-flat width, d is the total water depth on the reef flat (tidal level plus wave setup) and g is the gravitational acceleration. Becker et al. [11] conducted an EOF analysis of the wave measurements at the two reefs, and found that the dominant low-frequency variability on the reef flat can be characterized as a fundamental ($n = 0$) mode. We also find that wave energy within the IG band at S4 has a peak around the fundamental modal frequency of the reef oscillation based on our numerical results (Figs. 10d and 11d). To verify the occurrence of the excitation of reef normal modes, we alternatively compute the transfer function [e.g., 9, 56], which is defined as the ratio of the amplitude of the cross-spectrum between the envelope at S1 and the timeseries at S4, and the auto-spectra of the envelop at S1. The transfer function (Figs. 10f and 11f) shows a strong gain of energy around the fundamental frequency, consistent with a modal response near the shoreline to the envelope forcing.

4.2. Shoreline wave response to the shape variation of surf zone bathymetry

As indicated in Fig. 1, for either of the two reefs, there is a region (the cross-shore distance is about 50m) on the fore-reef slope where direct measurement of the seabed elevation is impractical due to the surf zone turbulence, thus a plane slope obtained by linear interpolation is simply used instead for that region. To address the effect of such bathymetric uncertainty on the shoreline responses of waves, we conducted four additional runs by assuming a combination of two types of arc profiles (convex and concave) and two values of arc curvature K (0.001 and 0.002). The variations of SS wave height (H_{SS}), IG wave height (H_{IG}) and wave setup ($\overline{\eta}_r$) near the shoreline (S4) with different profile shapes for the 1.5-hour events of CMI793 and ROI51 are shown in Fig. 12, Fig. 13, respectively.
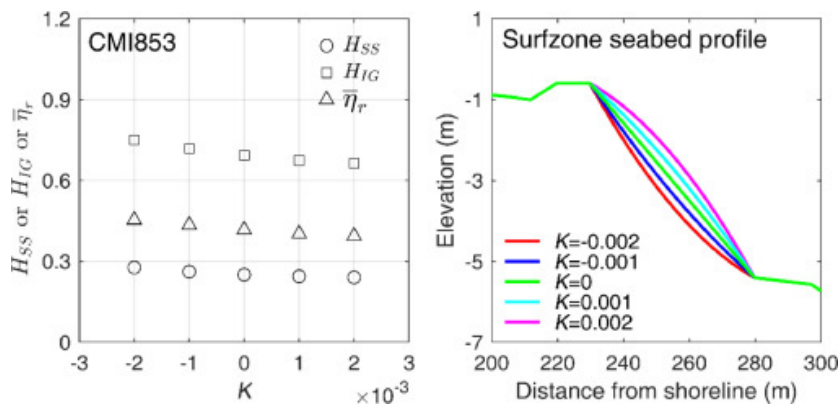
Fig. 12. SS wave height (H_{SS}), IG wave height (H_{IG}) and wave setup ($\overline{\eta}_r$) near the shoreline (S4) with different values of the curvature (K) of seabed profile in the surf zone for the CMI853 event.
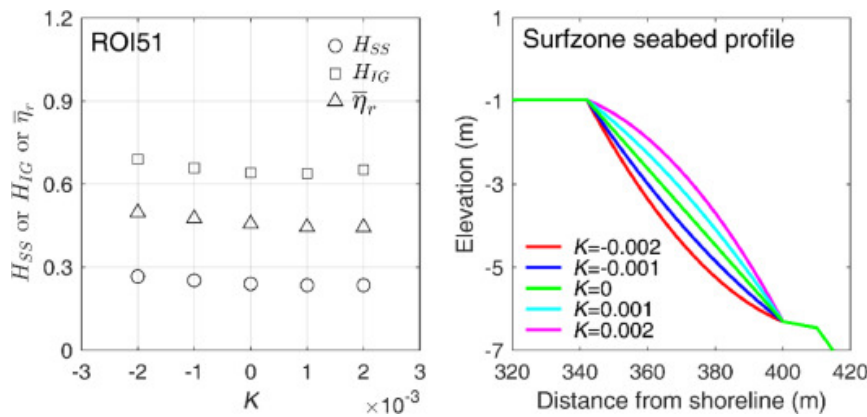
Fig. 13. The same as Fig. 12 but for the ROI51 event.

For the two events, all H_{SS}, H_{IG} and $\overline{\eta}_r$ slightly decrease as the profile shape varies from concave to convex, implying that shoreline <u>wave runup</u> with a concave surf zone profile is consistently larger than that with the convex profile. However, the values of H_{SS}, H_{IG} and $\overline{\eta}_r$ generally vary within 5% as the arc radius (inverse of K) doubles (i.e., from 500m to 1000m), indicating that the shoreline response of waves is not very sensitive to the surf zone bathymetry change, and the assumption of the linear plane slope in our previous simulations is satisfactory for shoreline runup estimation.

Fig. 14, Fig. 15 demonstrate the cross-shore distributions of wave height and mean water level for the shape variations simulations. The simulated wave records at any location across the reef profile are decomposed into the incoming (incident) and outgoing (reflective) signals using the method of Guza (1984) based on the wave and velocity records at that location. The concave/convex profile is equivalent to a steep/mild slope. A milder slope (larger K) can dissipate more SS waves by moving the incipient breaking point further seaward (Figs. 14a and 15a) thus it extends the surf zone and increases the frictional dissipation. Meanwhile, a steeper slope (smaller K) tends to generate more IG waves (Figs. 14c and 15c) by increasing the rate of depth-limited shortwave breaking (hence the efficiency of breakpoint forcing mechanism as discussed in Section 4.1). It also generates more wave setup on the reef flat by narrowing the surf zone (thus the gradient of radiation stress), see Figs. 14e and 15e. However, IG

wave reflection is significant seaward of the fore-reef slope (also found by Buckley et al. [57]) and wave reflection decreases (thus H_{IG} increases) as the slope becomes milder (Figs. 14d and 15d). These mechanics compensate for the decrease of H_{IG} with increase of K, which can explain the observations in Figs. 12 and 13 that the decrease of H_{IG} lessens as the slope becomes more convex.
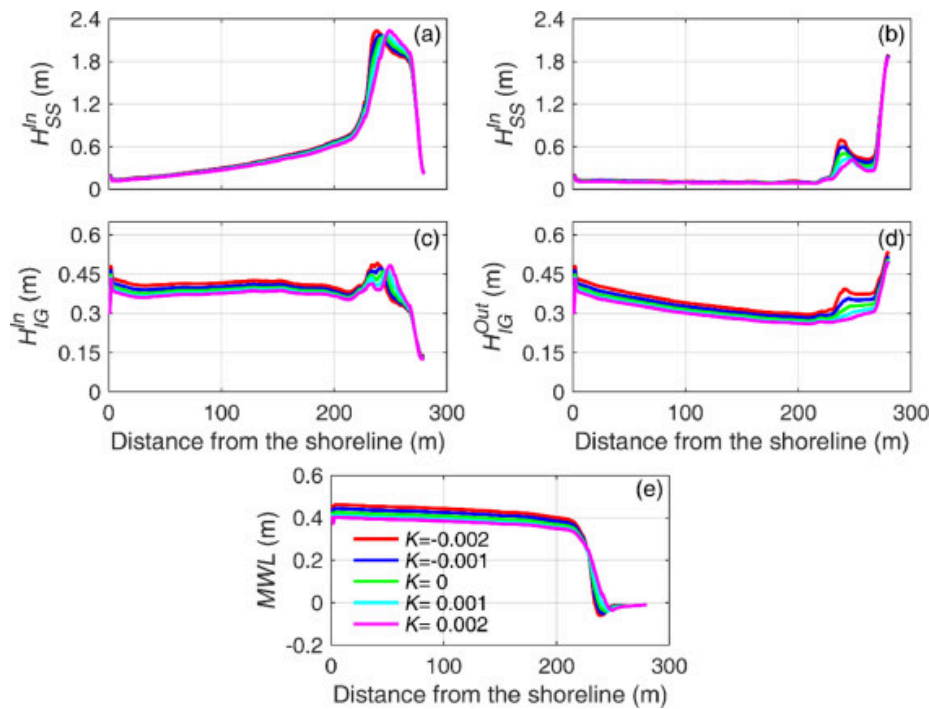
Download: Download high-res image (461KB)

Download: Download full-size image

Fig. 14. Incoming and outgoing SS wave heights (H_{SS}^{In} and H_{SS}^{Out}), IG wave heights (H_{IG}^{In} and H_{IG}^{Out}) and mean water level (MWL) across the reef with different values of the curvature (K) of seabed profile in the surf zone for the CMI853 event.
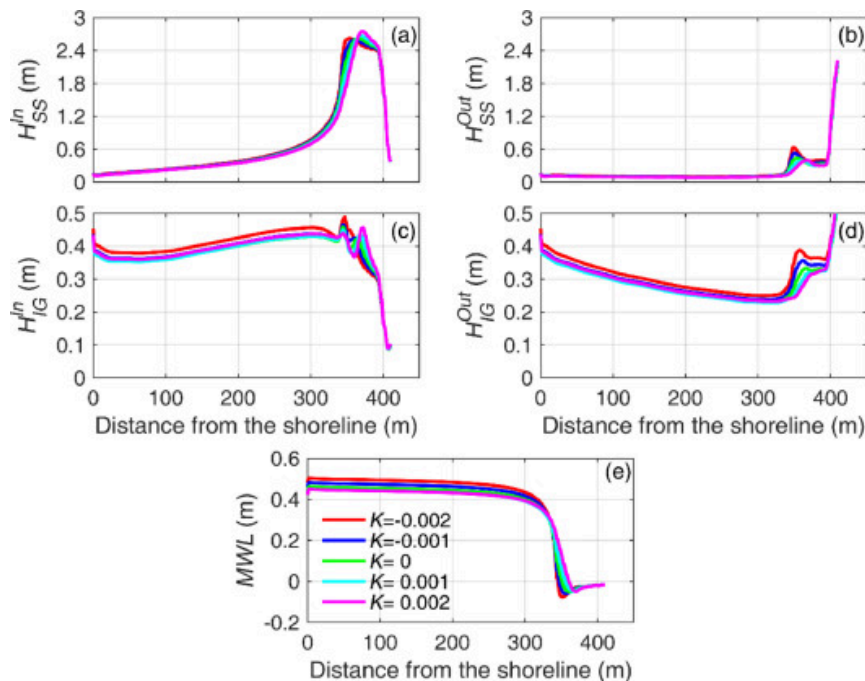
Download: Download high-res image (441KB)

Fig. 15. The same as Fig. 14 but for the ROI51 event.

4.3. Shoreline wave response to the phase variation of incident wave forcing

We have imposed the measured time-series of free surface elevation at the fore-reef slope location (S1) as the model input for the wave events simulated in Table 1. However, when the model is used for prediction and forecast purposes under other extreme wave events or at other reefs where the fore-reef measurements are absent, a standard spectrum (JONSWAP or TMA spectrum) typically is used in the model to generate the incident wave time series [30]. In this case, the bulk statistical wave parameters such as the significant wave height and peak wave period generally are required. Theoretically, a given wave spectrum has no phase information, and may be generated from a variety of time series with differing phases. As a result, the shoreline response of waves to the random phase variation of incident waves at the fore-reef slope is an open question.

The 1.5-hour events of CMI853 and ROI51 again are taken as examples to assess how the phasing of the incident time series affects wave transformation across the reef. For each event, new times series are determined by randomizing the phase of the Fourier amplitudes of the measured time series at S1 using a uniform distribution for the random phase. We generate 200 time series of the randomly-phased wave records and each time series is run successively as the model input. Table 4 presents the maximum values, minimum values, mean values and standard derivations of H_{SS}, H_{IG} and $\overline{\eta}_r$ near the shoreline (S4) obtained from N runs for both reefs. No significant difference could be found as N increases from 150 to 200, suggesting that our 200 runs are sufficient to show the effect of random phase.

Table 4. Maximum values (max), minimum values (min), mean values (ave) and standard derivations (std) of the SS wave height (H_{SS}), IG wave height (H_{IG}) and wave setup ($\overline{\eta}_r$) near the shoreline (S4) obtained from N runs using random-phased time series at S1 on the fore-reef slope as the numerical input.

(max, min, ave, std)	$N = 50$	$N = 100$	$N = 150$	$N = 200$
H_{SS} in CMI853	(0.280, 0.250, 0.268, 0.006)	(0.281, 0.250, 0.268, 0.006)	(0.296, 0.250, 0.267, 0.006)	(0.296, 0.250, 0.268, 0.006)
H_{IG} in CMI853	(0.900, 0.693, 0.802, 0.055)	(0.900, 0.678, 0.794, 0.050)	(0.915, 0.678, 0.794, 0.048)	(0.915, 0.678, 0.795, 0.048)
$\overline{\eta}_r$ in CMI853	(0.429, 0.405, 0.418, 0.005)	(0.429, 0.405, 0.418, 0.005)	(0.430, 0.401, 0.418, 0.005)	(0.430, 0.401, 0.417, 0.005)
H_{SS} in ROI51	(0.309, 0.285, 0.296, 0.006)	(0.309, 0.276, 0.295, 0.006)	(0.313, 0.276, 0.295, 0.006)	(0.313, 0.276, 0.295, 0.006)
H_{IG} in ROI51	(0.890, 0.641, 0.765, 0.052)	(0.890, 0.632, 0.765, 0.051)	(0.925, 0.615, 0.757, 0.058)	(0.925, 0.615, 0.756, 0.056)
$\overline{\eta}_r$ in ROI51	(0.482, 0.456, 0.469, 0.005)	(0.483, 0.456, 0.470, 0.005)	(0.483, 0.456, 0.470, 0.005)	(0.483, 0.456, 0.470, 0.005)

Fig. 16a and b show H_{SS}, H_{IG} and $\overline{\eta}_r$ at S4 for all 200 runs as well as their mean values and error bars for the two events, respectively. The error bars are determined by their standard deviations among the runs. The results show that H_{IG} is more sensitive to the phase change than H_{SS} and $\overline{\eta}_r$, particularly for the reef at ROI. The maximum H_{IG} (indicating the extreme shoreline wave height) among these runs is 0.915 m/0.925 m for CMI/ROI reef, which is

15.1%/22.5% larger than its mean value. The variations (standard derivations) in SS wave height and wave setup are generally less than 0.006, but they reach up to 0.056 for IG wave height (see the last column of Table 4). This can be explained by the fact that the IG wave response at the shoreline is related to the envelope of incident wave forcing as previously discussed. By taking the runs with maximum, median and minimum H_{IG} as examples, the spectra of the timeseries at S1 are identical among the runs as prescribed (Figs. 17a and 18a), but by randomizing the phase, the SS wave group envelopes differ (Figs. 17b and 18b). Larger H_{IG} corresponds to the run with envelope spectrum that is more energetic within the IG band as indicated by Figs. 17b and 18b. As SS wave breaking and the associated wave setup generation are mainly controlled by the depth-limited breaking on the reef flat, and the effects of phase variation on their shoreline responses are insignificant. Thus, phase variation of incident SS waves affects the SS wave envelope in the surf zone, which in turn affects the IG wave height at the shoreline.
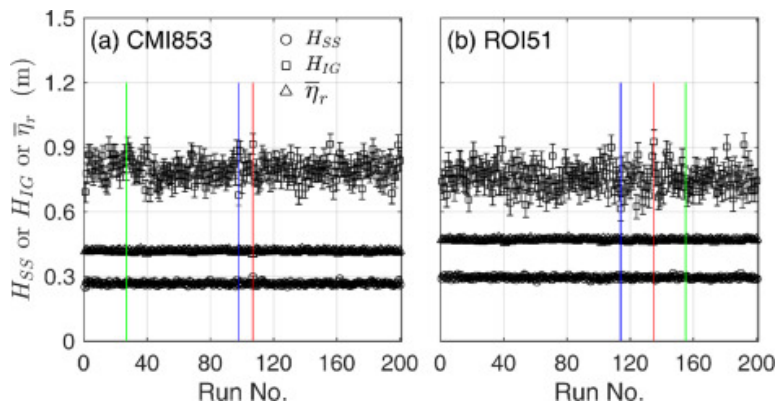
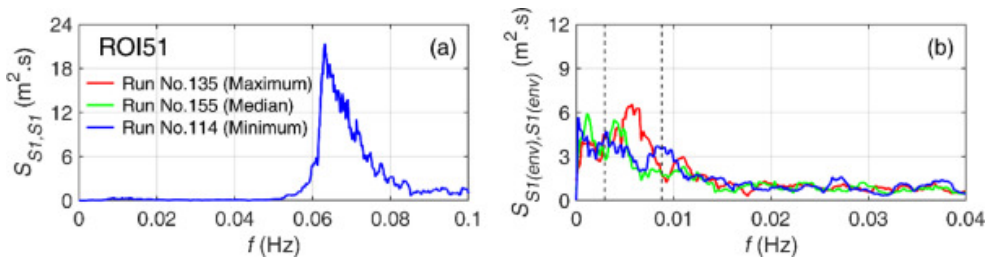Download: Download high-res image (338KB)

Download: Download full-size image

Fig. 16. SS wave height (H_{SS}), IG wave height (H_{IG}) and wave setup ($\overline{\eta}_r$) near the shoreline (S4) obtained from 200 runs using random-phased time series at S1 on the fore-reef slope as the numerical input. Color solid lines correspond to those runs shown in Figs. 17 and 18.
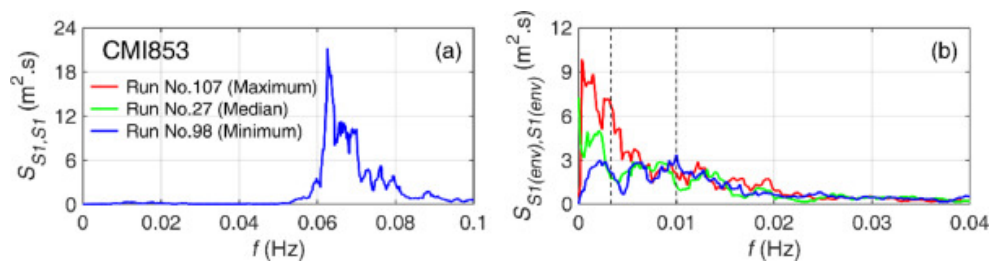
Download: Download high-res image (219KB)

Download: Download full-size image

Fig. 17. (a) Spectra of time-series of free surface elevations at S1 on the fore-reef slope based on three selective runs for the CMI853 event; (b) Spectra of the envelope of time-series of free surface elevations at S1 on the fore-reef slope based on the runs with maximum, median and minimum H_{IG} for the CMI853 event. The vertical dotted lines denote the first two theoretical resonant frequencies, respectively.

Download: Download high-res image (222KB)

Download: Download full-size image

Fig. 18. The same as Fig. 17 but for the ROI51 event.

4.4. Extreme water level estimation near the shoreline

For both CMI and ROI, Merrifield at al. [2] developed a parameterization for the shoreline extreme water level, which is related to that defined by Stockdon et al. [58] as the 2% exceedance water level at the shoreline above the still water level ($R_{2\%}$). Their empirical estimation gives

$$R_{2\%} = \bar{\eta}_r + 0.25b\sqrt{H_{SS}^2 + H_{IG}^2} \tag{11}$$

with a fitted value of $b = 2.2$ based on the combined CMI and ROI measurements. Merrifield at al. [2], however, analyzed the measurements at S4 near the shoreline, which was still about 50 m from the shoreline. They also suggest as future work to extend the extreme water level estimate to the region just prior to reaching the shoreline. Motivated by their suggestion, we extend the 2% exceedance water level estimation to shoreline, i.e., at a cross-shore distance of 5 m from the shoreline, via the numerical simulations. We believe that $R_{2\%}$ obtained at this location is a good proxy for the shoreline run-up considering that the beach slope at the shoreline is very steep (1:2.3 for CMI and 1:3.7 for ROI) at both reef sites (see also Fig. 1). Based on the wave events in Table 1, $R_{2\%}$ in this study is estimated as the 2% exceedance level of 1 Hz surface elevations for each bin (30-min records), with the tides removed.

The simulated $R_{2\%}$ at both 50 m and 5 m from the shoreline are plotted against the observed $R_{2\%}$ at 50 m from the shoreline in Fig. 19a. For most event bins at the two reefs, the predicted values of $R_{2\%}$ from 50 m to 5 m from the shoreline increase slightly, which is consistent with the spatial structure of mode $n = 0$ in Section 4.1. However, this shoreward increase in $R_{2\%}$ is generally less than 3%. For all event bins, the correlation coefficients the of predicted $R_{2\%}$ between the two locations are 0.98 for CMI reef and 0.94 for ROI reef, respectively. In addition, following Merrifield at al. [2], we combine all CMI and ROI event bins, and show in Fig. 19b the comparison between the predicted $R_{2\%}$ with the calculated $R_{2\%}$ based on Eq.(11) at both 50 m and 5 m from shoreline, respectively. The parameter b in Eq.(11) is obtained by a best fit of the predicted $R_{2\%}$ against the predicted H_{SS}, H_{IG} and $\bar{\eta}_r$ based on the combined data, which gives the $b = 2.6$ and 2.5 for 50 m and 5 m locations, respectively, with both coefficients of determination (r^2) larger than 0.8. These values of b are larger than the aforementioned $b = 2.2$ obtained by Merrifield at al. [2] possibly due to the fact that we only reproduce a very limited events (see Table 1) of their field observations. Nevertheless, all above analyses support the argument that wave measurements at a location 50 m from the shoreline as conducted by Merrifield at al. [2] can be satisfactorily used to analyze the shoreline wave run-up at these two reefs.
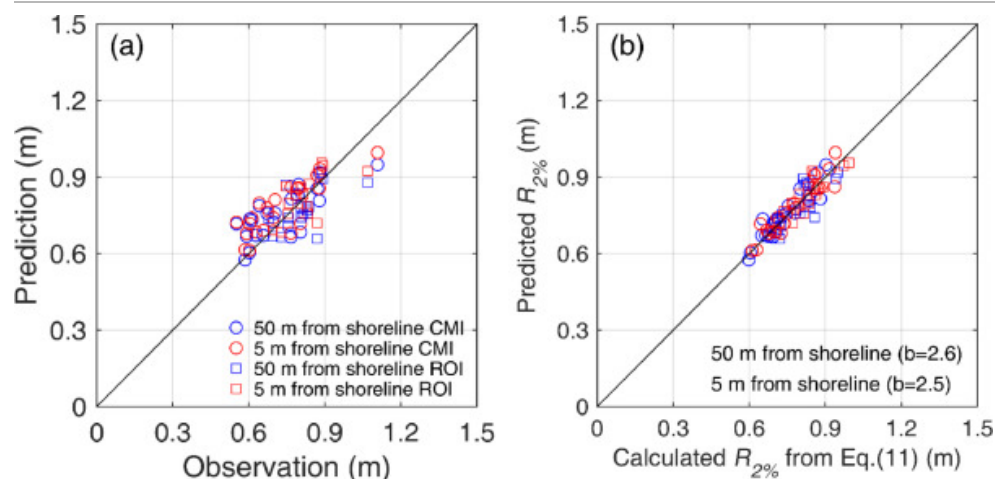
Fig. 19. (a) Predicted 2% exceedance water level ($R_{2\%}$) at both 50m and 5m from the shoreline vs. observed $R_{2\%}$ at 50m from the shoreline for all CMI event bins and all ROI event bins; (b) Predicted $R_{2\%}$ vs. calculated $R_{2\%}$ based on Eq.(11) at 50m and 5m from the shoreline for the combined CMI and ROI event bins.

5. Conclusions

To reproduce the cross-shore wave dynamics associated with wave-driven coastal run-up for fringing reefs, a 1DH numerical model based on the weakly dispersive, fully nonlinear Boussinesq-type equations with a finite-volume-based solver have been calibrated using field observations during energetic events. It is found that the model satisfactorily reproduces the cross-shore variations of SS and IG wave heights, wave spectra as well as mean water level over the two realistic reef sites in the Republic of the Marshall Islands. A cross-reef uniform Manning coefficient is found to be sufficient to represent the reef surface roughness for all wave events investigated.

By analyzing the numerical results, the SS wave group envelope is confirmed to be a good indicator of the cross-shore breakpoint forcing. IG waves are shown to be generated by the breakpoint forcing mechanism and the fundamental cross-shore mode is preferentially excited across the reef flat. Subsequent model applications show that SS waves, IG waves and wave setup with a concave surf zone seabed profile are generally larger than those with a convex profile. The effect of profile curvature within the tested range on the shoreline wave responses is insignificant, and model predictions based on the plane slope are representative. IG waves near the shoreline are more sensitive to the phase variation in incident wave forcing than SS waves and wave setup due the effects of phase on the incident wave group envelopes. The random phase simulations demonstrate that the extreme values of IG wave height may be approximately 20% larger than the mean values estimated from the random phase experiments. Since IG waves tend to be a dominant contributor to runup at reef-fringed shorelines, lack of information of incident wave phase contributes to model uncertainties in specifying runup. Lastly, we find that extreme water levels at 50m from the shoreline provide a satisfactory measure of extreme levels to within at least 5m of the shoreline, and can serve as a proxy for wave runup.

The present numerical results show that the model used in this study effectively simulates wave transformation over realistic fringing reefs, and provides an alternative tool to assess wave-driven coastal inundation around low-lying atolls during large wave events. Wave transformation over natural reefs is a complicated process, and we remark that cross-shore or alongshore currents, or inhomogeneity of the reef surface roughness, for example, may potentially affect wave processes over reefs in ways that may not be captured by a 1DH model. Further studies can

be directed to more refined investigations of the wave transformation through physical or numerical simulations using appropriate mathematical models.

Acknowledgments

Appendix A

The second-order terms D^c and D^x are expressed as:

$$D^c = -\frac{\partial}{\partial x}\left[(\eta+h)\left\{\left(\frac{(\eta^2-\eta h+h^2)}{6} - \frac{z_\alpha^2}{2}\right)\frac{\partial S}{\partial x} + \left(\frac{(\eta-h)}{2} - z_\alpha\right)\frac{\partial T}{\partial x}\right\}\right] \tag{A.1}$$

$$D^x = \frac{1}{2}\frac{\partial}{\partial x}\left(z_\alpha^2 u_\alpha \cdot \frac{\partial S}{\partial x}\right) + \frac{\partial}{\partial x}\left(z_\alpha u_\alpha \cdot \frac{\partial}{\partial x}T\right) + \left(T\frac{\partial T}{\partial x}\right)$$
$$-\frac{1}{2}\frac{\partial}{\partial x}\left(\eta^2 \frac{\partial S}{\partial t}\right)$$
$$-\frac{\partial}{\partial x}\left(\eta\frac{\partial T}{\partial t}\right) + \frac{1}{2}z_\alpha^2\frac{\partial^2 S}{\partial t\partial x} + z_\alpha\frac{\partial^2 T}{\partial t\partial x} - \frac{1}{2}\frac{\partial}{\partial x}\left(\eta^2 u_\alpha \cdot \frac{\partial S}{\partial x}\right)$$
$$-\frac{\partial}{\partial x}\left(\eta u_\alpha \cdot \frac{\partial T}{\partial x}\right) + \frac{\partial}{\partial x}\left(\frac{1}{2}\eta^2 S^2\right) + \frac{\partial}{\partial x}(\eta T S) \tag{A.2}$$

where S and T are given by

$$S = \frac{\partial}{\partial x}(U_0) \tag{A.3}$$

$$T = h\frac{\partial}{\partial x}(U_0) \tag{A.4}$$

and U_0 is the streamwise velocity

$$U_0 = U_0(x,t) \tag{A.5}$$

Recommended articles

References

[1]   R.K. Hoeke, K.L. McInnes, J.C. Kruger, R.J. McNaught, J.R. Hunter, S.G. Smithers
        Widespread inundation of Pacific islands triggered by distant-source wind-waves
        Global Planet. Change, 108 (2013), pp. 128-138
        🔴 View PDF   View article   View in Scopus ↗   Google Scholar ↗

[2]   M.A. Merrifield, J.M. Becker, M. Ford, Y. Yao
        Observations and estimates of wave-driven water level extremes at the Marshall Islands
        Geophys. Res. Lett., 41 (2014), pp. 7245-7253
        View in Scopus ↗   Google Scholar ↗

[3]   C.D. Storlazzi, S.B. Gingerich, A.V. Dongeren, O.M. Cheriton, P.W. Swarzenski, E. Quataert, C.I. Voss, D.W. Field, H. Annamalai, G.A. Piniak, R. McCall

Most atolls will be uninhabitable by the mid-21st century because of sea-level rise exacerbating wave-driven flooding

Sci. Adv., 4 (2018)

eaap9741

Google Scholar ↗

[4]   W.H. Munk, M.C. Sargent

Adjustment of Bikini atoll to ocean waves

Trans. Am. Geophys. Union, 29 (1948), pp. 855-860

Crossref ↗   View in Scopus ↗   Google Scholar ↗

[5]   R.W. Brander, P.S. Kench, D.E. Hart

Spatial and temporal variations in wave characteristics across a reef platform, Warraber Island, Torres Strait, Australia

Mar. Geol, 207 (2004), pp. 169-184

🔴 View PDF   View article   View in Scopus ↗   Google Scholar ↗

[6]   T.A. Hardy, I.R. Young

Field study of wave attenuation on an offshore coral reef

J. Geophys. Res. Oceans, 101 (1996), pp. 14311-14326

View in Scopus ↗   Google Scholar ↗

[7]   A. Lugo-Fernández, H.H. Roberts, J.N. Suhayda

Wave transformations across a Caribbean fringing-barrier coral reef

Cont. Shelf Res., 18 (1998), pp. 1099-1124

🔴 View PDF   View article   View in Scopus ↗   Google Scholar ↗

[8]   M.L. Buckley, R.J. Lowe, J.E. Hansen, A.R.V. Dongeren

Wave setup over a fringing reef with large bottom roughness

J. Phys. Oceanogr., 46 (2016), pp. 2317-2333

View in Scopus ↗   Google Scholar ↗

[9]   A.C.N. Péquignet, J.M. Becker, M.A. Merrifield, J. Aucan

Forcing of resonant modes on a fringing reef during tropical storm Man-Yi

Geophys. Res. Lett., 36 (2009), p. L03607

View in Scopus ↗   Google Scholar ↗

[10]   A. Pomeroy, R. Lowe, G. Symonds, A.V. Dongeren, C. Moore

The dynamics of infragravity wave transformation over a fringing reef

J. Geophys. Res. Oceans, 117 (2012), p. C11022

View in Scopus ↗   Google Scholar ↗

[11]   J.M. Becker, M.A. Merrifield, H. Yoon

Infragravity waves on fringing reefs in the tropical Pacific: dynamic setup

J. Geophys. Res. Oceans., 121 (2016), pp. 3010-3028

View in Scopus ↗   Google Scholar ↗

[12]   O.M. Cheriton, C.D. Storlazzi, K.J. Rosenberger

Observations of wave transformation over a fringing coral reef and the importance of low frequency waves and offshore water levels to run-up, overwash, and coastal flooding

J. Geophys. Res. Oceans, 121 (2016), pp. 3121-3140

View in Scopus ↗   Google Scholar ↗

[13]   O. Nwogu, Z. Demirbilek
Infragravity wave motions and runup over shallow fringing reefs
J. Waterw. Port Coastal Ocean Eng., 136 (2010), pp. 295-305

View in Scopus ↗   Google Scholar ↗

[14]   Y. Yao, Q.M. Zhang, S.G. Chen, Z.J. Tang
Effects of reef morphology variations on wave processes over fringing reefs
Appl. Ocean Res., 82 (2019), pp. 52-62

View PDF   View article   View in Scopus ↗   Google Scholar ↗

[15]   M.S. Longuet-Higgins, R.W. Stewart
Radiation stresses in water waves; a physical discussion, with applications
Deep-Sea Res, 11 (1964), pp. 529-562

View PDF   View article   View in Scopus ↗   Google Scholar ↗

[16]   S.B. Kraines, T. Yanagi, M. Isobe, H. Komiyama
Wind-wave driven circulation on the coral reef at Bora Bay, Miyako Island
Coral Reefs., 17 (1998), pp. 133-143

View in Scopus ↗   Google Scholar ↗

[17]   P. Douillet, S. Ouillon, E. Cordier
A numerical model for fine suspended sediment transport in the southwest lagoon of New Caledonia
Coral Reefs, 20 (2001), pp. 361-372

View in Scopus ↗   Google Scholar ↗

[18]   R.J. Lowe, J.L. Falter, S.G. Monismith, M.J. Atkinson
A numerical study of circulation in a coastal reef-lagoon system
J. Geophys. Res., 114 (2009), p. C06022, 10.1029/2008JC005081 ↗

View in Scopus ↗   Google Scholar ↗

[19]   R.J. Lowe, C. Hart, C.B. Pattiaratchi
Morphological constraints to wave-driven circulation in coastal reef-lagoon systems: a numerical study
J. Geophys. Res., 115 (2010), p. C09021, 10.1029/2009JC005753 ↗

View in Scopus ↗   Google Scholar ↗

[20]   A. Torres-Freyermuth, I. Mariño-Tapia, C. Coronado, P. Salles, G. Medellín, A. Pedrozo-Acuña, R. Iglesias-Prieto
Wave-induced extreme water levels in the Puerto Morelos fringing reef lagoon
Nat. Hazards Earth Syst. Sci., 12 (2012), pp. 3765-3773

Crossref ↗   View in Scopus ↗   Google Scholar ↗

[21]   A.V. Dongeren, R. Lowe, A. Pomeroy, D.M. Trang, D. Roelvink, G. Symonds, R. Ranasinghe
Numerical modeling of low frequency wave dynamics over a fringing coral reef
Coastal Eng, 73 (2013), pp. 178-190

Google Scholar ↗

[22]   E. Quataert, C. Storlazzi, A.V. Rooijen, O. Cheriton, A.V. Dongeren
       The influence of coral reefs and climate change on wave-driven flooding of tropical coastlines
       Geophys. Res. Lett., 42 (2015), pp. 6407-6415

       View in Scopus ↗   Google Scholar ↗

[23]   M. Postacchini, F. Lalli, F. Memmola, A. Bruschi, D. Bellafiore, I. Lisi, M. Brocchini
       A model chain approach for coastal inundation: application to the bay of Alghero
       Estuar. Coast. Shelf Sci., 219 (2019), pp. 56-70

       View PDF   View article   View in Scopus ↗   Google Scholar ↗

[24]   A. Sheremet, J.M. Kaihatu, S.F. Su, E.R. Smith, J.M. Smith
       Modeling of nonlinear wave propagation over fringing reefs
       Coast Eng, 58 (2011), pp. 1125-1137

       View PDF   View article   View in Scopus ↗   Google Scholar ↗

[25]   G. Ma, S.F. Su, S. Liu, J.C. Chu
       Numerical simulation of infragravity waves in fringing reefs using a shock-capturing non-
       hydrostatic model
       Ocean Eng, 85 (2014), pp. 54-64

       View PDF   View article   View in Scopus ↗   Google Scholar ↗

[26]   G. Franklin, I. Mariño-Tapia, A. Torres-Freyermuth
       Effects of reef roughness on wave setup and surf zone currents
       J. Coast Res, 65 (2013), pp. 2005-2010

       Crossref ↗   View in Scopus ↗   Google Scholar ↗

[27]   C. Skotner, C.J. Apelt
       Application of a Boussinesq model for the computation of breaking waves. Part 2: wave-induced
       setdown and set-up on a submerged coral reef
       Ocean Eng., 26 (1999), pp. 927-947

       View PDF   View article   View in Scopus ↗   Google Scholar ↗

[28]   Y. Yao, Z.H. Huang, S.G. Monismith, E.Y.M. Lo
       1DH Boussinesq modeling of wave transformation over fringing reefs
       Ocean Eng., 47 (2012), pp. 30-42

       View PDF   View article   View in Scopus ↗   Google Scholar ↗

[29]   S. Zhang, L. Zhu, J. Li
       Numerical simulation of wave propagation, breaking, and setup on steep fringing reefs
       Water, 10 (2018), p. 1147, 10.3390/w10091147 ↗

       View in Scopus ↗   Google Scholar ↗

[30]   Y. Yao, J.M. Becker, M.R. Ford, M.A. Merrifield
       Modeling wave processes over fringing reefs with an excavation pit
       Coast Eng., 109 (2016), pp. 9-19

       View PDF   View article   View in Scopus ↗   Google Scholar ↗

[31]   Y. Ning, W.J. Liu, X.Z. Zhao, Y. Zhang, Z.L. Sun
       Study of irregular wave run-up over fringing reefs based on a shock-capturing Boussinesq model

Appl. Ocean Res., 84 (2019), pp. 216-224

[PDF] View PDF   View article   Google Scholar ↗

[32]   V. Roeber, K.F. Cheung, M.H. Kobayashi
Shock-capturing Boussinesq-type model for nearshore wave processes
Coast. Eng., 57 (2010), pp. 407-423

[PDF] View PDF   View article   View in Scopus ↗   Google Scholar ↗

[33]   V. Roeber, K.F. Cheung
Boussinesq-type model for energetic breaking waves in fringing reef environments
Coast. Eng., 70 (2012), pp. 1-20

[PDF] View PDF   View article   View in Scopus ↗   Google Scholar ↗

[34]   Y. Yao, F. He, Z.J. Tang, Z.S. Liu
A study of tsunami-like solitary wave transformation and run-up over fringing reefs
Ocean Eng., 149 (2018), pp. 142-155

[PDF] View PDF   View article   View in Scopus ↗   Google Scholar ↗

[35]   S.F. Su, G. Ma, T.W. Hsu
Boussinesq modeling of spatial variability of infragravity waves on fringing reefs
Ocean Eng., 101 (2015), pp. 78-92

[PDF] View PDF   View article   View in Scopus ↗   Google Scholar ↗

[36]   S.F. Su, G. Ma
Modeling two-dimensional infragravity motions on a fringing reef
Ocean Eng., 153 (2018), pp. 256-267

[PDF] View PDF   View article   View in Scopus ↗   Google Scholar ↗

[37]   T. Shimozono, Y. Tajima, A.B. Kennedy, H. Nobuoka, J. Sasaki, S. Sato
Combined infragravity wave and sea-swell runup over fringing reefs by super typhoon Haiyan
J. Geophys. Res., 120 (2015), pp. 4463-4486, 10.1002/2015JC010760 ↗

View in Scopus ↗   Google Scholar ↗

[38]   J.M. Becker, M.A. Merrifield, M. Ford
Water level effects on breaking wave setup for Pacific Island fringing reefs
J. Geophys. Res. Oceans, 119 (2014), pp. 914-932

View in Scopus ↗   Google Scholar ↗

[39]   P. Lynett, P.L.F. Liu
Modeling wave generation, evolution, and interaction with depth-integrated
Dispersive Wave Equations. Coulwave Code Manual v.2.0, Cornell Univ, Ithaca, New York (2008)

Google Scholar ↗

[40]   M. Filippini, A.G. Kazolea, M. Ricchiuto
A flexible genuinely nonlinear approach for nonlinear wave propagation, breaking and runup
J. Comput. Phys., 310 (2016), pp. 381-417

View in Scopus ↗   Google Scholar ↗

[41]   D. Clamond, D. Dutykh, D. Mitsotakis
Conservative modified Serre-Green-Naghdi equations with improved dispersion characteristics
Commun. Nonlinear Sci., 45 (2017), pp. 245-257

    View PDF   View article   View in Scopus ↗   Google Scholar ↗

[42]   M. Kazolea, M. Ricchiuto

On wave breaking for Boussinesq-type models

Ocean Model, 123 (2018), pp. 16-39

    View PDF   View article   View in Scopus ↗   Google Scholar ↗

[43]   J.S.A. Do Carmo, J.A. Ferreira, L. Pinto

On the accurate simulation of nearshore and dam break problems involving dispersive breaking waves

Wave Motion, 85 (2019), pp. 125-143

    View PDF   View article   View in Scopus ↗   Google Scholar ↗

[44]   O. Nwogu

Alternative form of Boussinesq equations for nearshore wave propagation

J. Waterw. Port Coastal Ocean Eng. ASCE, 119 (1993), pp. 618-638

View in Scopus ↗   Google Scholar ↗

[45]   D.H. Kim, P. Lynett, S.A. Socolofsky

A depth-integrated model for weakly dispersive, turbulent, and rotational fluid flows

Ocean Modeling, 27 (2009), pp. 198-214

    View PDF   View article   View in Scopus ↗   Google Scholar ↗

[46]   M. Tonelli, M. Petti

Hybrid finite volume–finite difference scheme for 2DH improved Boussinesq equations

Coastal Eng, 56 (2009), pp. 609-620

    View PDF   View article   View in Scopus ↗   Google Scholar ↗

[47]   F. Shi, J.T. Kirby, J.C. Harris, J.D. Geiman, S.T. Grilli

A high-order adaptive time-stepping TVD solver for Boussinesq modeling of breaking waves and coastal inundation

Ocean Model, 43 (2012), pp. 36-51

    View PDF   View article   View in Scopus ↗   Google Scholar ↗

[48]   A.B. Kennedy, Q. Chen, J.T. Kirby, R.A. Dalrymple

Boussinesq modeling of wave transformation, breaking, and runup. I: 1D

J. Waterw. Port Coastal Ocean Eng. ASCE, 126 (2000), pp. 43-50

Google Scholar ↗

[49]   A.O. Akan

Normal-flow. Open Channel Hydraulics

Elsevier, Butterworth Heinemann Press, Oxford, UK (2006), pp. 67-96

    View PDF   View article   Google Scholar ↗

[50]   G. Wei, J.T. Kirby, A. Sinha

Generation of waves in boussinesq models using a source function method

Coastal Eng, 36 (1999), pp. 271-299

    View PDF   View article   View in Scopus ↗   Google Scholar ↗

[51]   J.T. Kirby, G. Wei, Q. Chen, A.B. Kennedy, R.A. Dalrymple

FUNWAVE1.0: Fully Nonlinear Boussinesq Wave Model Documentation and User's Manual

Center for Applied Coastal Research, University of Delaware (1998)

Google Scholar ↗

[52]   P.J. Lynett, T.R. Wu, L.F. Liu

Modeling wave runup with depth-integrated equations

Coast. Eng., 46 (2002), pp. 89-107

📄 View PDF   View article   View in Scopus ↗   Google Scholar ↗

[53]   Y. Yao, Z.J. Tang, C.B. Jiang, W.R. He, Z.S. Liu

Boussinesq modeling of solitary wave run-up reduction by emergent vegetation on a sloping
beach

J. Hydro-Environ. Res., 19 (2018), pp. 78-87

📄 View PDF   View article   View in Scopus ↗   Google Scholar ↗

[54]   C.J. Willmott

On the validation of models

Phys. Geog., 2 (1981), pp. 184-194

Crossref ↗   View in Scopus ↗   Google Scholar ↗

[55]   A.C.N. Péquignet, J.M. Becker, M.A. Merrifield

Energy transfer between wind waves and low-frequency oscillations on a fringing reef, Ipan,
Guam

J. Geophys. Res. Oceans., 119 (2014), pp. 6709-6724

View in Scopus ↗   Google Scholar ↗

[56]   M. Gawehn, A.V. Dongeren, A.V. Rooijen, C.D. Storlazzi, O.M. Cheriton, A. Reniers

Identification and classification of very low frequency waves on a coral reef flat

J. Geophys. Res. Oceans., 121 (2016), pp. 7560-7574

View in Scopus ↗   Google Scholar ↗

[57]   M.L. Buckley, R.J. Lowe, J.E. Hansen, A.R.V. Dongeren, C.D. Storlazzi

Mechanisms of wave-driven water level variability on reef-fringed coastlines

J. Geophys. Res. Oceans, 123 (2018), pp. 3811-3831

Crossref ↗   View in Scopus ↗   Google Scholar ↗

[58]   H.F. Stockdon, R.A. Holman, P.A. Howd, A.H. Sallenbury

Empirical parameterization of setup, swash, and runup

Coast. Eng., 53 (2006), pp. 573-588

📄 View PDF   View article   View in Scopus ↗   Google Scholar ↗

Cited by (12)

Numerical simulation of interaction between wave-driven currents and revetment on coral reefs

2022, Ocean Engineering

Citation Excerpt :

…Boussinesq-type equations were adopted by including porosity and resistance terms to mirror the drag force generated by
mangroves, whose ability to dampen waves helps minimize damage from caused catastrophic events such as erosive wave

attacks, torrential storms, and tsunamis (Kamil et al., 2021). To better understand the cross-shore wave dynamics associated with coastal wave run-up, Yao et al. (2020b) developed a weakly dispersive numerical model based on the one-dimensional horizontal (1DH) and highly nonlinear Boussinesq equations. This numerical model was then applied to the two realistic fringing reefs with different reef configurations and roughness characteristics in the Republic of the Marshall Islands....

Show abstract ⌄

Uncertainty of wave runup prediction on coral reef-fringed coasts using SWASH model

2021, Ocean Engineering

Citation Excerpt :

...An alternative approach is to deduce the hydraulic roughness from in-situ measurements based on wave frictional dissipation theories (e.g., Nelson, 1996; Pomeroy et al., 2012), but accurate reproduction of reef roughness is still challenging in both numerical and physical modelings. Nonhydrostatic- and Boussinesq-type numerical models, which have high efficiency in simulating intra-wave processes, often adopt the Manning or Chezy formulae to account for the resistance effect although they are proposed initially for unidirectional flows (e.g., Nwogu and Demirbilek, 2010; Ning et al., 2019; Yao et al., 2020; Zijlema et al., 2011). The accurate formula between hydraulic roughness height and the Manning and Chezy coefficient values for oscillation flows has not been established and demands comprehensive investigations in the future....

Show abstract ⌄

Physical and numerical modeling of random wave transformation and overtopping on reef topography

2021, Ocean Engineering

Citation Excerpt :

...Except for the SWs, infragravity waves (IGWs) (0.004–0.04 Hz in prototype) also contribute largely to the water-level fluctuations and the consequent coastal flooding. Despite their secondary magnitude in off-reef regions, interactions between incident waves and reef topographies highly promote the IGWs on the reef flat (Buckley et al., 2018; Cheriton et al., 2016; Masselink et al., 2019; Nwogu and Demirbilek, 2010; Yao et al., 2019), because the steep fore-reef slope is favorable to the generation of moving-breakpoint forced IGWs which are more energetic than the released bound IGWs (Masselink et al., 2019; Yao et al., 2020b). Phases and heights of the generated free IGWs are subsequently modified by the reflection processes at both the shoreline (or seawall) and the reef edge....

Show abstract ⌄

Wave-Driven Hydrodynamic Processes Over Fringing Reefs With Varying Slopes, Depths, and Roughness: Implications for Coastal Protection ↗

2022, Journal of Geophysical Research Oceans

An early warning system for wave-driven coastal flooding at Imperial Beach, CA ↗

2021, Natural Hazards

On the small-scale fractal geometrical structure of a living coral reef barrier ↗

2020, Earth Surface Processes and Landforms

> View all citing articles on Scopus ↗

View Abstract